Fly ash waste-derived Fe@Fe$_3$O$_4$ core-shell nanoparticles for acetic acid ketonization

Sasha Yang [a], Binbin Qian [a,b], Yuan Wang [c,d], Kenji Taira [a], Qiaoqiao Zhou [a], Karen Wilson [d], Adam F. Lee [d], Lian Zhang [a,*]

[a] *Department of Chemical and Biological Engineering, Monash University, Wellington Road, Clayton, Melbourne, Victoria 3800, Australia*
[b] *School of Chemistry and Environmental Engineering, Yancheng Teachers University, Yancheng 224002, China*
[c] *Institute for Frontier Materials, Deakin University, Victoria 3125, Australia*
[d] *Centre for Advanced Materials & Industrial Chemistry (CAMIC), School of Science, RMIT University, Melbourne, Victoria 3000, Australia*

ABSTRACT

Iron oxide is a cost-effective catalyst for the ketonization of carboxylic acid components of bio-oil crude derived from the pyrolysis of lignocellulosic biomass. Fly ash (FA) waste from coal-fired power plants is an abundant source of iron oxide precursors. Here we report the reductive thermal processing of hematite derived from acid-leached fly ash. Annealing of the hydroxide precipitated leachate produces nanoparticulate α-Fe$_2$O$_3$ containing ~10 wt% metal impurities (principally Al, Mg, Ca and Ti). Subsequent extended (5 h) reduction under H$_2$ at 400 °C generates a Fe@Fe$_3$O$_4$ core-shell structure, and is accompanied by surface segregation of Al, Mg, Ca and Ti as their oxides, a decrease in particle size, and the concomitant formation of surface oxygen vacancies. These physicochemical changes increase the surface area and introduce Brønsted basicity alongside the intrinsic Lewis acidity of the non-stoichiometric magnetite, promoting ketonization through synergistic activation of two acetic acid molecules. The specific activity of the 5 h reduced FA derived catalyst (FA-5 h) was 3.9 mmol·g^{-1}·min^{-1} at 400 °C, with a corresponding turnover frequency per acid site of 14.3 min^{-1}. In-situ DRIFTS reveals acetic acid dissociatively adsorbs over FA-5 h, adopting a bidentate acetate binding mode identical to that for commercial magnetite, albeit the fly ash derived catalyst stabilises acetate to a higher temperature (~300 °C) facilitating C-C coupling versus desorption. Successive doping of commercial magnetite by low concentrations of Al, Mg, Ca and Ti, and subsequent reduction, generated a model catalyst whose acid-base properties and ketonization activity reproduced those of FA-5 h. Surface segregated dopants, notably Ti, are largely responsible for the high activity of FA-5 h through the introduction of additional acid and base sites for acetic acid ketonization.

1. Introduction

Bio-oils derived from the pyrolysis of lignocellulosic waste can be upgraded to yield renewable fuels to support the global transition to a Net Zero carbon dioxide emission future [1]. Unfortunately, despite such promise, pyrolysis bio-oils are ill-suited for direct use due to an abundance of carboxylic acids, which are corrosive, result in oil instability, and also lower the oil heating value [2,3]. Several strategies are proposed to upgrade oxygenated primary bio-oils into more stable, energy-rich deoxygenated alkanes, with ketonization one of the simplest to implement. In ketonization, two carboxylic acids are reacted together, accompanied by the elimination of a CO$_2$ and water molecule, as illustrated in Scheme 1 for acetic acid [4,5]. In contrast to other deoxygenation strategies, ketonization does not require either molecular H$_2$ or a H-donor molecule (as for hydrodeoxygenation and transfer hydrogenation), and hence is more atom economical, although the loss of a carbon atom in the CO$_2$ by-product is undesirable. Nevertheless, in the example of acetic acid, ketonization halves the oxygen content (from a C:O molar ratio of 1:1 to 2:1 in acetone).

A broad range of metal oxides has been examined as heterogeneous catalysts for both gas and liquid phase ketonization. Basic oxides such as MgO, CaO and BaO, which are readily reduced, and amphoteric oxides like CeO$_2$, ZrO$_2$, MnO$_2$, TiO$_2$ and Al$_2$O$_3$ with stronger M-O bonds, are reported to offer high activity, selectivity and stability [6–12]. The 2030 United Nations Sustainable Development Goals have focused societal interest on improved resource utilisation, and in catalysis a desire to

identify earth-abundant elements to drive chemical transformations. Iron (and its oxides) have a high natural abundance in the Earth's crust, low toxicity and cost, and are produced on the megaton scale annually as bauxite residue (often termed Red Mud, a waste by-product of the Bayer process to manufacture alumina) which is rich in hematite (α-Fe_2O_3). Industrial waste containing iron oxides is a thus promising candidate for exploitation in new catalytic technologies. Metallic Fe powder was first reported for the ketonization of light fatty acids (Fig. 1), wherein ferrous carboxylate and hydrogen were observed [13] with a decomposition of ferrous carboxylate into ferrous oxide speculated as a potential route to a catalytic cycle. Indeed, Murzin and co-workers observed that steel reaction vessels can catalyse ketonization in the absence of any other catalyst [14]. Numerous studies have focused on reagent-grade iron oxide catalysts, including reduced hematite [15], pure [16] or silica-supported magnetite (Fe_3O_4) [17], and hematite doped with Si, Cr or K [18]. These catalysts exhibit comparable (and even superior) activity to precious metals and rare earth oxides. For example, silica-supported Fe_3O_4 proceeded with a similar rate of acetic acid ketonization to that of Ru/TiO_2 or CeO_2 catalysts at 400 °C [6,7,17]. The literature consensus is that magnetite is more active than hematite (Fe_2O_3) due to a higher concentration of vacancies sites [4,19] and associated acidity of the former; Brønsted basic and Lewis acid sites have both been invoked in ketonization reaction mechanisms [4,20]. Basic sites are believed to coordinate primary reaction intermediates such as adsorbed carboxylates, facilitating subsequent α-hydrogen abstraction or ketoenol tautomerisation to generate an adsorbed enolate, with neighbouring coordinatively unsaturated (Lewis acid) cations activating a second carboxylic acid molecule to effect C-C coupling [4]. Transition metal dopants can alter and affect the physicochemical properties of metal oxide catalysts, notably the number of oxygen vacancies and coordinatively unsaturated cations, and corresponding acid-base and redox character [4]. The preceding work has driven research on the reduction and acid treatment of Fe-rich Red Mud to produce a magnetite active phase for gas-phase ketonization. Elhamet al [21] confirmed the necessity of reduction to activate Red Mud as a catalyst for the ketonization and deoxygenation of alkanoic acids and levulinic acid. Reduced Red Mud most likely forms Fe_3O_4, though reduced iron silicates and/or carbides have not been discounted. Co-existing TiO_2, silica and alumina phases may act as acid/base co-catalysts and/or promoters of iron oxide phases. Justin et al. [19] reported that Ca, Na and K promoted the activity and stability of reduced Red Mud for ketonization of fast pyrolysis oil derived oxygenates, by introducing solid basicity. However, very high catalyst reduction temperatures lower ketone selectivity and yield, likely caused by textural changes alongside a loss of acid/base sites. Clearly, fundamental insight into structure-reactivity relations for iron containing waste materials has to date been hindered by the plethora of inorganic impurities present (including Al, Si, Ti, Ca, Mg and Na), whose roles and synergies as catalyst promoters and/or poisons requires systematic study.

Here, we report the synthesis of a Fe@Fe_3O_4 core-shell catalyst derived from Fe-rich fly ash, an abundant, global waste resource. In contrast to Red Mud, wherein acid washing is used to remove impurities from the iron-rich residue [19], acid washing was used by us to selectively extract an Fe^{3+}-rich leachate from fly ash [23] for subsequent precipitation and thermal processing. Annealing and thermal reduction result in the formation of a defective magnetite shell comprising ~80 nm crystallites around 180 nm metallic iron cores, and surface

segregates the main metal impurities (Al, Mg, Ti and Ca) as their oxides. The combination of Lewis acidity and Brønsted basicity enables the efficient activation of acetic acid for vapour phase catalytic ketonization to acetone with good stability for 10 h on-stream. In-situ spectroscopic and model catalyst studies confirm (defective) magnetite as the active phase and highlight the role of surface impurities in enhancing both acid and base properties, and consequent activity, of the waste-derived materials for bio-oil upgrading.

2. Experimental

2.1. Materials

Coal fly ash (FA) was collected from the Energy Australia Yallourn power plant in Victoria, Australia. Chemicals including 32 wt% HCl, NaOH, Fe_2O_3, Fe_3O_4, acetic acid and $TiCl_4$ were obtained from Sigma-Aldrich in the highest available purity. Other analytical grade chemicals, including $FeCl_3$, $AlCl_3$ and $MgCl_2$ were also obtained from Sigma-Aldrich at 99.99% purity to synthesise (intentionally doped) hematite. Elemental analysis by ICP revealed the untreated fly ash predominantly comprised Fe_2O_3 and MgO (Table S1), with smaller quantities of CaO, alumina, silica and other trace metal oxides. Iron extraction from this fly ash sample has been previously detailed [23]. In brief, 2 g of coal fly ash (100–500 μm) was washed with 40 mL deionised water and then by 4 mL of 32 wt% HCl to extract ~80% of Fe into the leachate (Table S1), along with significant Mg and Ca.

2.2. Hematite synthesis from fly ash

The FA leachate was subjected to stepwise treatments summarised in Fig. 2 to generate ketonization catalysts (details provided in the Supporting Information). Note that this fly ash leachate is extremely lean in heavy metals such as V and Pd (undetectable by elemental analysis) or Ni and Cr (<0.01 ppm) [24,25]. In brief, the pH of the leachate was adjusted to ~3.6 by the addition of 2 M NaOH to precipitate Fe^{3+} as ferric hydroxide (Fe(OH)$_3$), which was subsequently washed with deionised water to remove residual contaminants. The washed precipitate was then heated to 400 °C under N_2 to yield α-Fe_2O_3, and finally reduced under flowing 10% H_2 at 400 °C (200 mL·min^{-1}, ramp rate 10 °C·min^{-1}) to obtain defective Fe_3O_4. Reduction of α-Fe_2O_3 is reported to exsolve interstitial or lattice impurities with different atomic radii to Fe^{3+} [26] from magnetite, thereby creating cationic and/or oxygen vacancies [27]. Fly ash derived reduced catalysts are designated FA-xh hereafter, where xh refers to the H_2 reduction time in hours. Catalysts were stored in a vacuum desiccator after reduction to avoid re-oxidation.

2.3. Synthesis of doped α-Fe_2O_3

The influence of different impurities on the physicochemical properties of synthetic α-Fe_2O_3 was examined by the deliberate addition of one or more of $AlCl_3$, $MgCl_2$, $CaCl_2$ or $TiCl_4$ to a $FeCl_3$ solution at similar concentrations to those observed in the fly ash derivative. Each mixed metal chloride solution, and a pure $FeCl_3$ solution, were precipitated at pH 3.6 by 2 M NaOH, heated to 400 °C under flowing N_2 and the flow then switched to 10% H_2 at 400 °C for 5 h. The resulting five new catalysts were designated. SFe-5 h for synthetic reduced Fe_2O_3; SFeAl-5 h
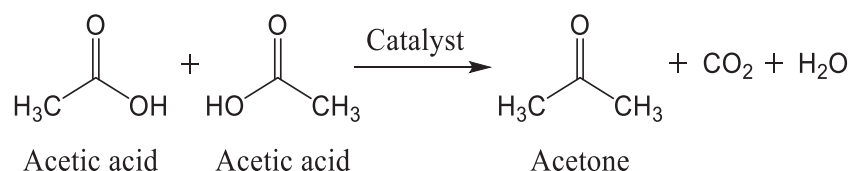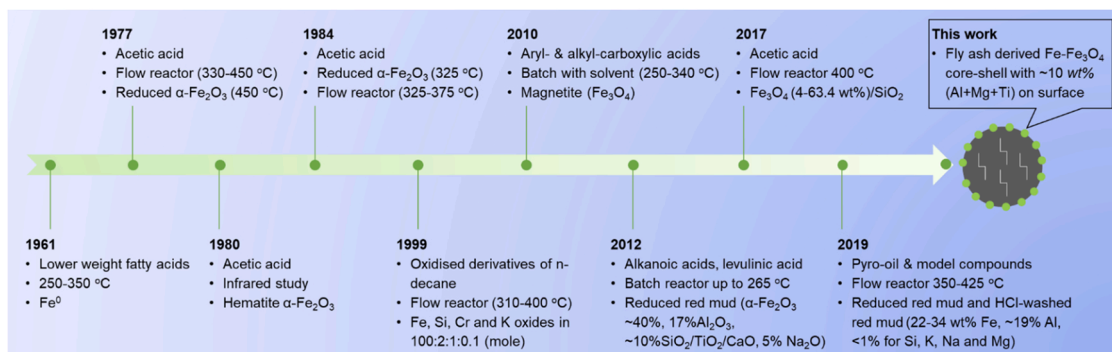

Scheme 1. Acetic acid ketonization.

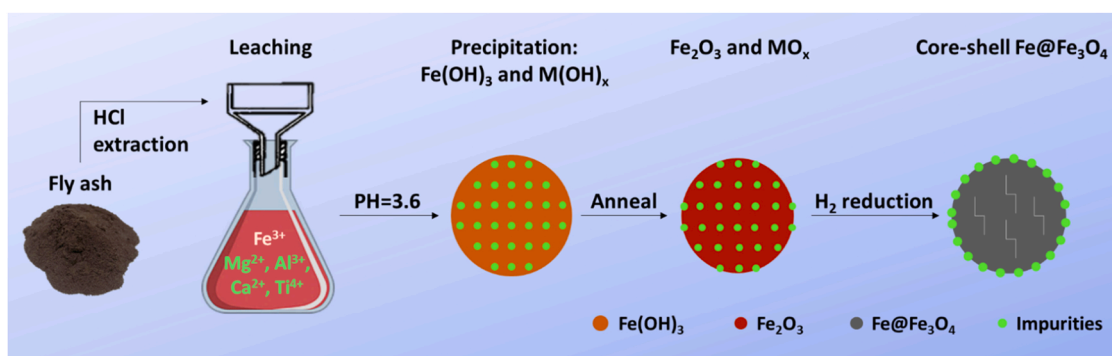**Fig. 1.** Historical overview of iron oxide catalysts for ketonization [13,15–19,21,22].

Fig. 2. Synthesis of Fe@Fe$_3$O$_4$ core-shell catalyst from coal fly ash. M indicates metal impurities.

for Al doped and reduced Fe$_2$O$_3$; SFeAlMg-5 h for Al and Mg doped and reduced Fe$_2$O$_3$; SFeAlMgCa-5 h for Al, Mg and Ca doped and reduced Fe$_2$O$_3$; and SFeAlMgCaTi-5 h for Al, Mg, Ca and Ti doped and reduced Fe$_2$O$_3$. In all cases, the dopant concentrations were chosen to match those in the fly ash derived α-Fe$_2$O$_3$.

2.4. Acetic acid ketonization

2.4.1. Pyroprobe screening

Catalysts were initially screened for the ketonization of pure acetic acid in a Pyroprobe reactor (CDS 5200) under a very fast heating rate (125–150 °C·s^{-1}) [28,29]. Approximately 1 mg of pre-reduced catalyst and 0.2 mg acetic acid were loaded in a quartz tube (2 mm i.d. x 25 mm). Quartz wool was placed between the catalyst and acetic acid to minimise their interaction before heating (Fig. S1(**a**)) Subsequently, the reactor was heated to the target temperature under flowing helium (>99.999%, 26 mL·min^{-1}) for 15 s, equating to a residence time of 0.37–0.56 s between 300 and 600 °C. Evolved gases were analysed by on-line GC (Gas Chromatography, Agilent 7890 B) fitted with thermal conductivity and flame ionisation (FID) detectors, as previously detailed [30]. Acetone yield was considered a measure of catalyst activity (calibration curve shown in Fig. S2). Injected samples were analysed in triplicate with error bars reported as twice the standard deviation.

2.4.2. Time-on-stream (TOS) ketonization studies

The optimal catalysts identified by screening on the Pyroprobe reactor were further studied for acetic acid ketonization using a plug flow quartz reactor (10 mm i.d. x 60 cm, Fig. S1(b)) and an electric tube furnace. Approximately 100 mg of catalyst was pre-mixed with 500 mg SiC (80 grit) and the resulting powder was positioned in the middle of the reactor tube between quartz wool plugs. Reactions were performed by flowing N$_2$ (200 mL·min^{-1}) through the catalyst bed during heating to 400 °C (ramp rate 10 °C·min^{-1}). The gas stream was then switched to 10% H$_2$ in N$_2$ for a 5 h in-situ catalyst reduction, before reverting to

flowing N$_2$ for 10 min to purge residual H$_2$. Acetic acid was then pumped using a programmable syringe pump upwards through the reactor, where it was vaporised and mixed with N$_2$ to make up a total gas flow rate of 200 mL·min^{-1}. Acetic acid vapour concentrations of 0.5 vol%, 1.5 vol% or 5 vol% were investigated, and the corresponding catalyst mass to acetic acid mass flow ratio (W/F, h) spanned 0.06–1.20 h similar to literature values of 0.095–4 h [19,31,32]. The reactor exit stream was heated at 120 °C to prevent acetic acid condensation, with the hot outlet gas passing through two impinger bottles containing a 100 mL Milli-Q water/dry ice mixture to trap condensates with the remaining vapour passing to an ETG 9500 FTIR CO$_2$ gas analyser. Condensed liquids were periodically sampled to quantify acetic acid and acetone by GC-FID. Quantitative analysis of individual products for representative reactions confirmed a CO$_2$:acetone molar ratio of 1:1, and corresponding carbon mass balance > 95% (Table S2). The vast majority of acetic acid underwent ketonization without significant by-product formation or carbonization; neither direct decarboxylation nor decarbonylation to methane or CO respectively [33] was observed (Fig. S3). Acetone percent yields were therefore continuously calculated by an indirect method based on the CO$_2$ product and initial acetic acid concentrations according to Eq. 1. Percent yields, i.e. the actual yield/ theoretical yield (x100%), were calculated from the mols of product formed relative to the maximum number of mols that would be obtained from complete and selective conversion of the acetic acid reactant. This definition recognises that unreacted feedstock is detrimental to the catalytic process.

$$
\begin{aligned}
\text{Acetone yield\%} &= \frac{\text{Actual mols acetone product}}{\text{Theoretical mols acetone product}} \times 100 \\
&= \frac{\text{CO}_2 \text{ at outlet(mol/min)}}{0.5 \times \text{Acetic acid at inlet(mol/min)}} \times 100
\end{aligned}
\tag{1}
$$

Specific activity is defined as the mols of acetic acid converted per g of catalyst per unit time; average specific activity (same units) is

calculated from the total mols of acetic acid converted during the first 120 min reaction.

Turnover frequencies (TOFs) were determined from the average (during the first 120 min of reaction) number of mols of acetic acid converted per min normalised to the mols of acid sites determined from NH_3-TPD.

$$TOF = \frac{\text{Average mols of acetic acid molecules reacted per min}}{\text{Mols of active sites}}$$

(2)

For experiments using the Pyroprobe microreactor, the acetone product was directly measured and hence the acetone yield was calculated from the mols of acetone relative to that expected from the stoichiometric reaction in Scheme 1 ($2CH_3COOH = C_3H_6O + CO_2 + H_2O$), for which the acetone yield should be half of the mols acetic acid placed into the reactor. For experiments using the plug flow reactor, for which acetic acid was continuously fed to the reactor, CO_2 was used as a proxy for acetone yield on the assumption that both were produced in equimolar amounts. As noted above, periodic sampling and GC-FID analysis of the actual acetone concentration confirmed this assumption. Acetic acid conversion in the plug flow reactor was also determined from the ratio of actual:theoretical CO_2 yields.

2.5. Catalyst characterization

Fresh, reduced and/or spent catalysts were stored in a vacuum desiccator before/after use and their bulk and surface physicochemical properties were extensively characterized (see **SI**). Analyses included N_2 porosimetry for BET (Brunauer-Emmett-Teller) surface areas, inductively coupled plasma mass spectroscopy (ICP-MS) for elemental compositions, X-ray diffraction (XRD) for crystallinity, scanning electron microscopy (SEM) and scanning transmission electron microscopy (STEM) for sample morphology, X-ray photoelectron (XPS) for surface composition and oxidation state, and Fe K-edge X-ray absorption near-edge spectroscopy (XANES) to determine the local oxidation state and chemical environment of Fe species. Catalyst acid-base properties were measured by NH_3 temperature-programmed desorption (NH_3-TPD), CO_2-TPD and pyridine chemisorption. Reaction mechanisms were investigated by in-situ diffuse reflectance infrared Fourier transform (DRIFTS). Reduced catalysts were wetted with 20 μL acetic acid, dried at 100 °C under flowing He (20 mL·min^{-1}) for 40 min to remove physisorbed acid and water, and then cooled to room temperature. Dried samples were then heated to 400 °C (ramp rate 5 °C·min^{-1}) during FTIR spectral acquisition; evolved gases were analysed by online mass spectrometry using a Hiden HPR20-R&D gas analysis system.

3. Results and discussion

3.1. Bulk and surface properties of fly ash derived materials

Elemental analysis of the precipitated (and annealed) FA leachate prior to H_2 reduction is shown in Table S3. Unsurprisingly, Fe_2O_3 dominates (89 wt%), with Al_2O_3 (6.9 wt%) the main impurity due to the existence of Al^{3+} in the leachate and the similar pH sensitivity of iron oxides and alumina to precipitation [23,34]. Trace alkaline earth oxides and TiO_2 were also present (0.75 wt% MgO, 0.35 wt% for CaO and 0.33 wt% TiO_2). The bulk composition was unaffected by annealing. The BET surface area of the precipitated FA was 199 m^2·g^{-1} (Table S3) due to the predominance of a low-density iron hydroxide phase (Fig. S4 (a)), similar to a literature report [35]. Annealing, and the resulting phase transition to ~1 μm α-Fe_2O_3 nanoparticles (Table S3) lowers the surface area to ~42 m^2·g^{-1}; albeit still far larger than that of commercial high-purity hematite (5 m^2·g^{-1}). The pore volume of the annealed FA is also greater than commercial hematite. Though not definitive, these textural differences could reflect the influence of impurity elements, in particular Al^{3+}, whose doping into hematite is known to increase the resulting surface area [36]. All reflections for annealed FA and commercial hematite were characteristic of α-Fe_2O_3; the absence of crystalline phases attributable to impurities indicates these were well-dispersed throughout the hematite lattice. Volume-averaged crystallite sizes (Table S3) from Scherrer analysis of the corresponding XRD patterns (Fig. S4(a)) are also smaller for the annealed FA precipitate than that of commercial hematite, consistent with their differing surface areas. Surface analysis by XPS (Fig. S4 (b)) confirmed the presence of Al, Mg, Ti and Ca in decreasing surface concentrations relative to Fe (Fig. S4 (c)). Table S4 shows a slight surface enrichment of the annealed FA precipitate in Al.

3.2. Effect of reduction

Reduced forms of iron oxide, notably magnetite, are reported as active for ketonization, hence the impact of thermal H_2 treatments on fly ash derived materials was investigated. Table 1 shows that H_2 reduction altered the properties of commercial hematite and the annealed FA precipitate, with the latter a strong function of reduction time. XRD analysis of these reduced materials (Fig. 3) reveals a rapid phase change to magnetite for the FA-derived material within the first hour of reduction (Fig. 3(a)), accompanied by the emergence of a metallic iron phase during extended reduction. Fe K-edge XANES spectra also evidenced a Fe^0 pre-edge feature at ~7115 eV, whose intensity increased with reduction time (Fig. 3(b)); least squares fitting to reference materials (Fig. S5) quantified the bulk metallic Fe^0 content which rose from 28 atom% to 97 atom% as the reduction time increased from 1 h to 5 h, with the remaining iron present as magnetite. These changes in iron speciation for the FA-derived material were accompanied by a significant rise in BET surface area (Table 1 and Fig. S6) and a concomitant fall in magnetite and Fe metal crystallite sizes indicative of nanoparticle fracturing. In contrast, Fe 2p XPS (Fig. 3(c)) only identified high valence iron surface species, which in combination with XRD and XANES results, evidence a $Fe@Fe_3O_4$ (magnetite) core-shell nanoparticle structure. Bulk and surface elemental analysis of FA derived materials reveals that the reduction of hematite to magnetite and metallic iron is accompanied by progressive surface segregation of the main impurities (Al, Ca, Mg and Ti) from the parent lattice and interstices [26,37,38]. This segregation may result from the co-migration of lattice oxygen anions (to fill surface oxygen vacancies) and the more oxophilic impurity cations [39]. In contrast, prolonged reduction of commercial hematite produced pure iron metal crystallites.

Quantitative analysis of surface compositions by XPS (Fig. 4, based on data in Table S5) confirms increasing surface segregation of impurity metals with reduction time. This implies a time-dependent outward diffusion of these impurity elements, which may be aided by progressive fracturing of the (annealed) fly-ash derived particles. TEM bright-field images of the FA-5 h material (Fig. 5a) show cuboidal particles of 100–400 nm diameter, whose cores are iron rich and possess shells of 20–100 nm thick enriched in metal impurities (Fig. 5(h-i)). These observations are consistent with the preceding X-ray measurements and the proposed $Fe@Fe_3O_4$(+impurity) core-shell structure. Metal impurities at the surface of FA-5 h were all in high oxidation states (Fig. S7). The Al, Ti and Ca 2p$_{3/2}$ binding energies of 74.2 eV, 458.8 eV and 347.2 eV, respectively, and Mg 1 s of 1304 eV, are indicative of their stable oxides (Al_2O_3, TiO_2, CaO and MgO), as expected due to the high oxophilicity of these elements [39]. Although mixed metal oxides such as $Fe_{2-x}Al_xO_3$ [38] or magnesium ferrite could also form, there is no evidence of such phases from XRD.

3.3. Catalytic activity evaluation

The impact of H_2 reduction on catalytic performance of reduced iron oxide materials was first examined for acetic acid ketonization in a Pyroprobe reactor. Fig. 6(a) reveals that neither reduced commercial hematite nor FA-3 h or FA-5 h materials was active < 300 °C, with their

Table 1
Properties of reduced fly ash derived samples.

Catalyst	Porosimetry		Crystallite size, nm		$\sum M^1/Fe$	Acidity[2] (mmol/g)			Basicity[3] (mmol/g)		
	S_{BET} m²/g	Pore volume (cm³/g)	Fe₃O₄	Fe⁰		Weak	Medium	Total	Weak	Medium	Total
CFe₂O₃-5 h	2	0.01	–	270	0.00	0.01	0.01	0.02	0.01	0.01	0.03
FA-1 h	30	0.25	94	–	1.58	0.26	0.12	0.38	0.02	0.01	0.03
FA-2 h	30	0.25	156	286	–	0.24	0.12	0.36	0.02	0.02	0.04
FA-3 h	31	0.27	130	219	1.67	0.18	0.13	0.31	0.02	0.03	0.05
FA-4 h	37	0.30	129	201	1.89	0.17	0.10	0.27	0.02	0.06	0.09
FA-5 h	40	0.27	80	188	2.22	0.14	0.13	0.27	0.01	0.09	0.10

[1] total metal impurities quantified by XPS surface scan

[2] NH₃-TPD;

[3] CO₂-TPD.
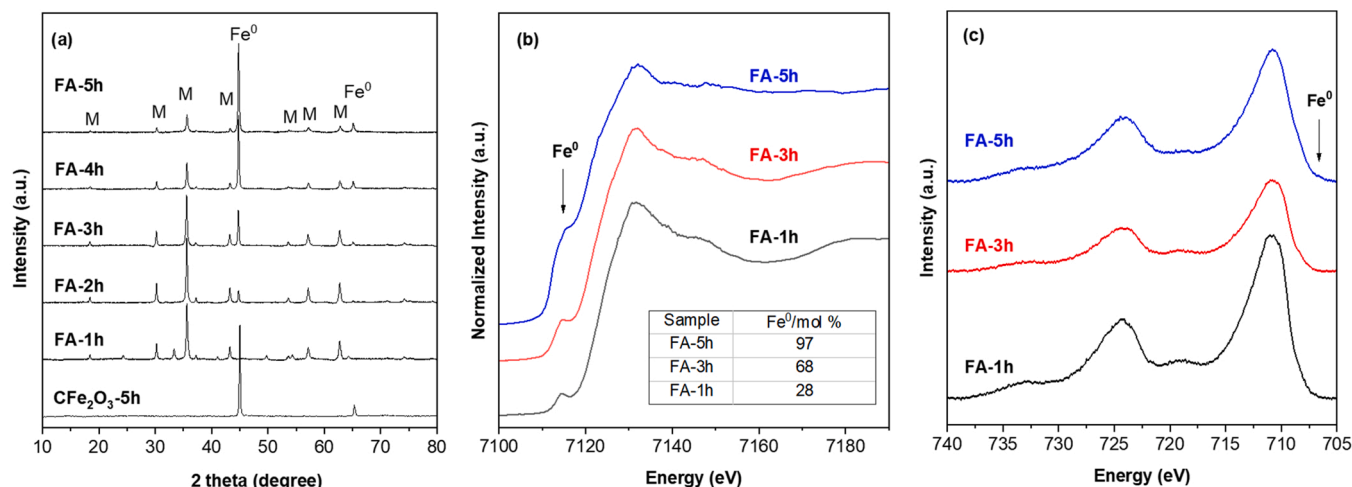
Fig. 3. (a) XRD patterns (M: magnetite), (b) Fe K-edge XANES and (c) Fe 2p XP spectra of fly ash derived catalysts with different duration reductive treatments.

activity reaching a (different) plateau between 400 °C and 600 °C. The FA-5 h material was the most active, producing ~75% of the maximum theoretical acetone yield, followed by FA-3 h and the reduced commercial hematite (CFe₂O₃-5 h); the latter only yielded ~18 mol% acetone indicating that metallic iron was a poor catalyst. Increasing reduction time induced a monotonic increase in the absolute and surface area normalised acetone yields for the FA-derived material (Fig. 6(b)). The latter observation demonstrates that enhanced ketonization is not a consequence of changes in textural properties (particle size) but rather the nature of the surface active site. Since magnetite forms during the first hour of reduction (Fig. 3(a)), the larger acetone yield at longer reduction times is likely associated with promotion by surface segregated impurities, notably Al and Ca whose evolving surface content (Fig. 5) mirrors acetone yields.
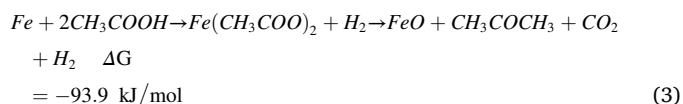
Reduced commercial hematite and FA-derived catalysts were subsequently subjected to more rigorous testing in a continuous plug flow microreactor. With regarding the reduced commercial hematite in Fig. 7 (a), it shows an initial burst of ketonization activity, but was rapidly deactivated within 120 min time-on-stream (TOS), albeit the deactivation rate was slower for the CFe₂O₃-5 h catalyst produced after the 5 h reduction. In comparison, the FA-5 h catalyst in Fig. 7(b) exhibited a greater maximum acetone yield than CFe₂O₃-5 h, which was maintained for 120 min TOS without any significant deactivation. The poor stability of CFe₂O₃-5 h may reflect surface coking (Table S6). Increasing the W/F ratio from 0.06 h to 1.20 h progressively increased the FA-5 h ketonization activity, such that complete acetic acid conversion and 100% acetone yield were achieved at the highest value, being maintained for 10 h TOS (Fig. 7 (c-d)). The TOF per surface acid site (Table 1) for FA-5 h was calculated as 14.3 min⁻¹, which is comparable to the literature values of 13 min⁻¹ for Fe₃O₄/SiO₂ [17], ~20 min⁻¹ for ZrO₂ [11], and
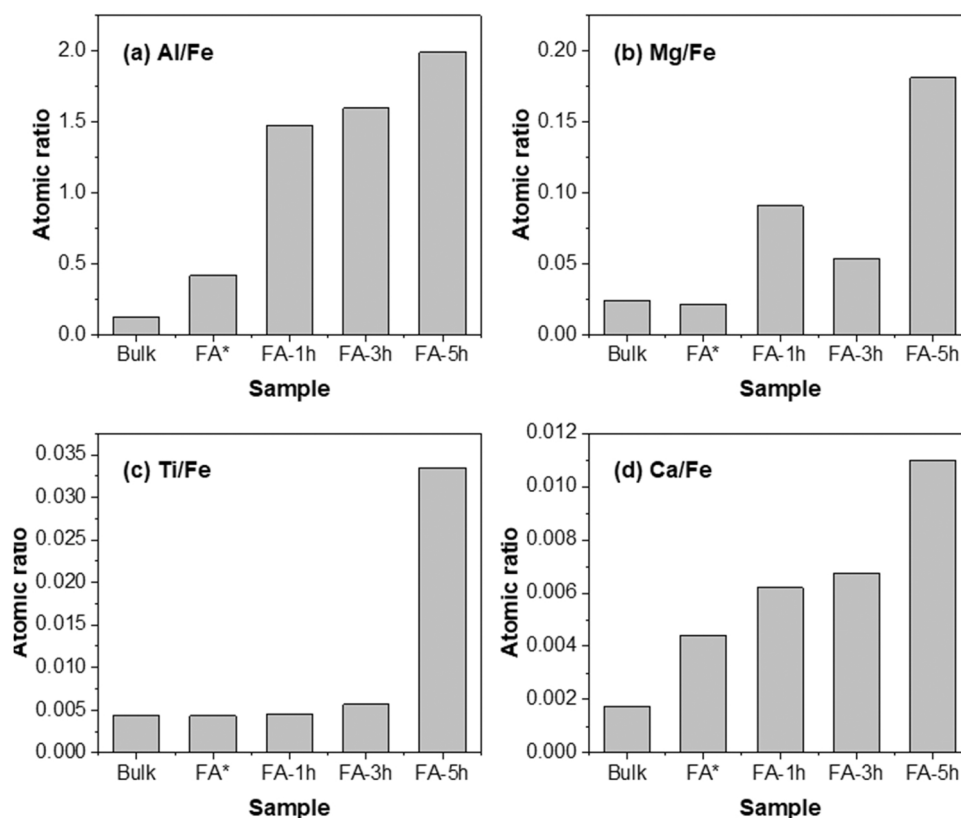
~5 min⁻¹ Ga-ZSM-5 [10]. Regarding the specific activity for acetic acid conversion, it reached over 3.9 mmol·g⁻¹·min⁻¹ for FA-5 h (Fig. S8), which outperformed reduced commercial hematite (CFe₂O₃-5 h, 2.5 mmol·g⁻¹·min⁻¹), although it was lower than that of untreated Red Mud (~30 mmol·g⁻¹·min⁻¹) which contains high levels of alkali contaminants [17].
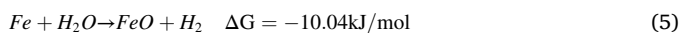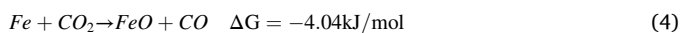
3.4. Model and mechanistic studies

3.4.1. Role of metallic Fe⁰ within the catalyst matrix

Iron speciation in metallic and oxidic forms during catalytic ketonization reaction was studied by X-ray analysis of the spent FA-5 h after 5 h acetic acid ketonization at 400 °C. X-ray analysis evidenced significant re-oxidation of the metallic iron iron core to magnetite (Fig. 8(a) and Fig. S9), with the extent of its oxidation being inversely proportional to the W/F ratio. Acetic acid [13,14] and/or reactively-formed H₂O and CO₂ kotonization products are the likely oxidants in accordance with Eqs. 3–5 below. Evolved gas products (H₂, CO and CO₂) from the reduced FA-5 h catalyst treated with either acetic acid or water at 400 °C were therefore studied in the Pyroprobe reactor (Fig. 8(b)). More hydrogen was produced from acetic acid than from pure water, suggesting that the former is a more effective oxidant of metallic iron and hence Eq. 5 can be discounted. In contrast, the observation of reactively-formed CO from Pyroprobe and the early stages of TOS experiments in the plug flow microreactor over CFe₂O₃-5 h and FA-5 h (Fig. 8(c)) support CO₂ as a potential oxidant (Eq. 4).

$$Fe + 2CH_3COOH \rightarrow Fe(CH_3COO)_2 + H_2 \rightarrow FeO + CH_3COCH_3 + CO_2$$
$$+ H_2 \quad \Delta G$$
$$= -93.9 \text{ kJ/mol} \tag{3}$$

Fig. 4. Relative bulk (ICP) and surface (XPS) content of impurity elements to Fe in reduced fly ash derived materials (Bulk and FA* are for the sample after annealing).

$$Fe + CO_2 \rightarrow FeO + CO \quad \Delta G = -4.04 kJ/mol \quad (4)$$

$$Fe + H_2O \rightarrow FeO + H_2 \quad \Delta G = -10.04 kJ/mol \quad (5)$$

Evolved H_2 gas is previously reported during carboxylic acid ketonization over iron powder [4], although CO was not observed. Elucidating the mechanism by which metallic iron cores are oxidised would require future operando XAS measurements to measure the kinetics of the metal to magnetite phase transformation. Nevertheless, it is likely that some form of Cabrera-Mott oxidation mechanism [40,41] operates, involving rapid oxidation of iron atoms/cations in contact with the magnetite layer, and subsequent slower diffusion of oxygen anions (supplied by acetic acid) driven by cation migration via place-exchange to the oxide surface. Such a growth mechanism can also be driven by the inward diffusion of oxygen vacancies (Kirkendall effect [42,43]) promoting the formation of core-void-shell nanostructures [44]. Reactant-driven restructuring of the parent Fe@Fe$_3$O$_4$ to magnetite-rich nanoparticles likely accounts for the high activity of FA-5 h for ketonization. Furthermore, post-reaction TEM imaging and EDX elemental mapping reveal that in-situ oxidation of the FA-5 h catalyst also improved particle dispersion, with sizes between 30 and 90 nm (Fig. S10) compared with 100–250 nm for the parent FA-5 h, while Al and Ti impurities remain localised at particle surfaces (Fig. S11).

The nature of active sites in reduced catalysts was also examined by XPS. O 1 s XPS spectra (Fig. S12) revealed a range of surface oxygen species characteristic of lattice oxygen (530 eV binding energy), oxygen vacancies (530.5 eV), hydroxyls (531.5 eV) and protonated water (532.5 eV) [45,46]. Neither reduced commercial hematite (CFe$_2$O$_3$-5 h) nor the unreduced fly ash derived catalysts possessed surface oxygen vacancies. However, the reduction of the fly ash derived catalyst induced surface oxygen vacancy formation, with a maximum concentration attained for FA-3 h and FA-5 h (Table 2). Since oxygen vacancies are associated with the formation of Lewis acid sites and may

synergistically catalyse ketonization [47,48], it is likely that the increase in ketonization activity with reduction temperature noted in Fig. 6(b) is at least partially attributable to oxygen vacancy formation. Our hypothesis that non-stoichiometric magnetite is the active phase responsible for acetic acid ketonization was further explored by reducing commercial high-purity Fe$_3$O$_4$ (99.999%, Sigma Aldrich) at 400 °C and screening in the Pyroprobe reactor (Fig. 9). Stoichiometric magnetite, though superior to hematite, was indeed almost inactive (only 5% acetone yield) suggesting it is not the principal active site for ketonization as previously postulated [15,49]. Magnetite reduction, quantified by the mass loss from temperature programmed reduction according to Fe$_3$O$_4$ + H$_2$ → Fe + H$_2$O, likely occurs stepwise through a range of FeO$_x$ intermediate phases accompanied by oxygen vacancy formation. The extent of magnetite reduction is strongly correlated with acetone yield for reduction times ≤ 2 h, consistent with our hypothesis that partially reduced (non-stoichiometric) magnetite catalyses acetic acid ketonization in our system. Loss of activity for the bulk magnetite after prolonged reduction of 3–5 h may reflect particle agglomeration and a loss of surface area. The most active 2 h reduced magnetite delivers significantly lower acetone yields than the FA-5 h catalyst, despite their similar Fe^0 contents; we attribute this to the higher surface area and/or presence of impurity promoters in the fly ash-derived catalyst.

In-situ DRIFTS studies confirmed that commercial magnetite and fly ash derived catalysts exhibited qualitatively similar surface chemistry (Fig. 10). At temperatures < 200 °C, acetic acid adopts a similar bridging bidentate acetate adsorption mode over CFe$_3$O$_4$, CFe$_3$O$_4$-2 h and FA-5 h, characterized by ν_{as}(COO), ν_{sym}(COO), and δ_s(CH$_3$) bands at 1540 cm^{-1}, 1430 cm^{-1} and 1343 cm^{-1} respectively [17,50–53]. All band intensities increased from CFe$_3$O$_4$ < CFe$_3$O$_4$-2 h << FA-5 h, mirroring their ketonization activity in Fig. 9, and exhibited similar temperature dependencies > 200 °C, characterized by a progressive loss of acetate. However, whereas surface acetate was fully desorbed/reacted over the parent and reduced commercial magnetites by
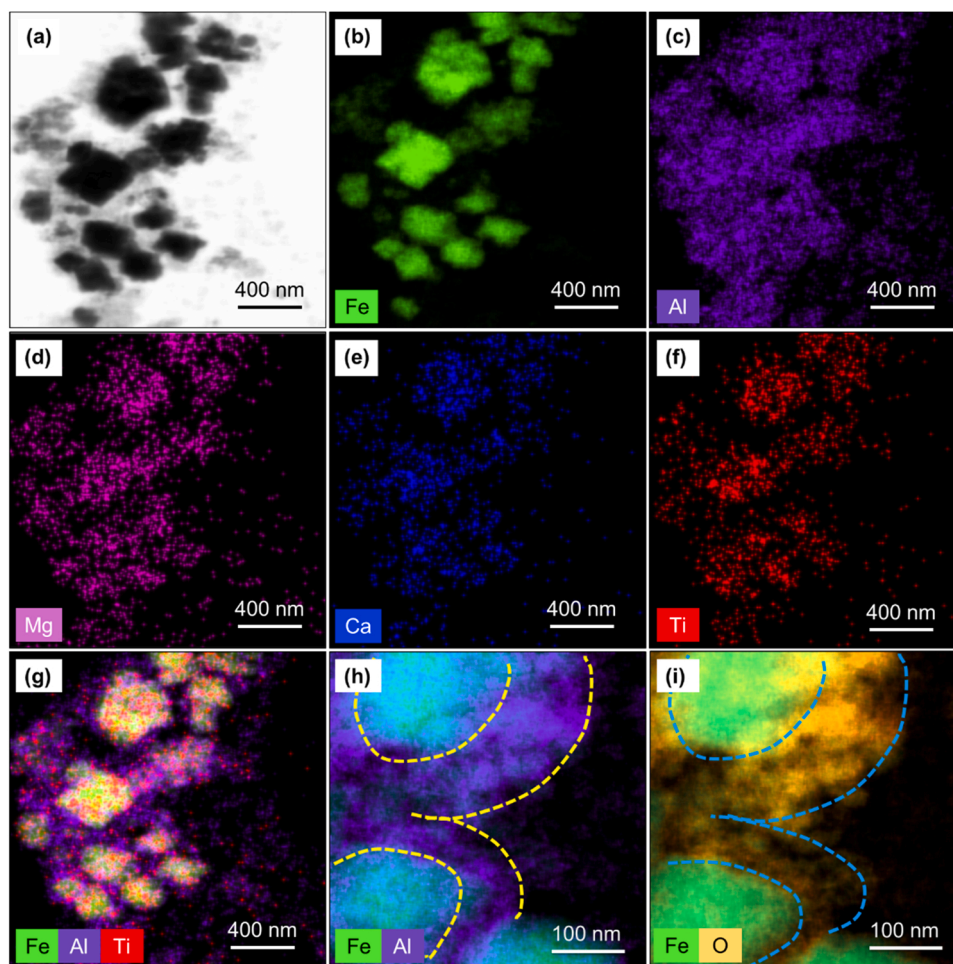
Fig. 5. (a) STEM-HAADF image of FA-5 h catalyst, and (b-i) corresponding elemental maps from EDX.
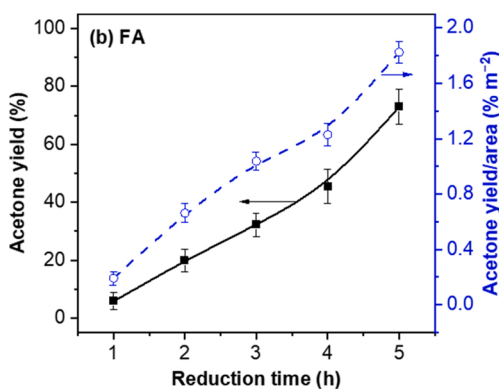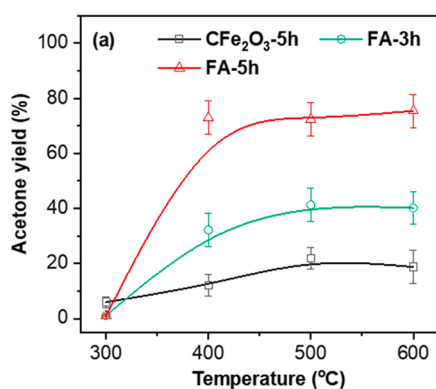

Fig. 6. (a) Acetone yield from acetic acid ketonization over reduced commercial and FA-derived iron oxide catalysts as a function of reaction temperature, and (b) absolute and surface area normalised acetone yields for FA-derived catalysts as a function of reduction temperature tested at 400 °C. All reactions were performed by rapid heating in a Pyroprobe system; acetone yields are cumulative from room temperature to the quoted reaction temperature, and were directly measured by GC-FID.

275 °C, a significant amount remained on the most active FA-5 h. We propose that the superior activity of the FA-5 h catalyst is associated with (Lewis acid) defect sites which are able to stabilize surface acetate at high temperatures under which direct ketonization (Scheme 1) is facile. Activation of surface acetate over FA-5 h > 200 °C is indicated by a blue shift in the $\nu_{as}(COO)$ band to ~1600 cm^{-1} and splitting of the $\delta_s(CH_3)$ band to yield a new feature at 1318 cm^{-1}, both changes absent for commercial magnetite. The latter 1318 cm^{-1} band might be associated with the $\delta_s(CH_3)$ band of acetate coordinated to surface segregated TiO$_2$ [20]. Online mass spectrometry confirmed that loss of surface acetate from FA-5 h > 200 °C coincided with the evolution of reactively-formed CO$_2$ and acetone (Fig. S13), which pass through a maximum around 300 °C; note the decline in ketonization products at higher temperatures simply reflects complete consumption of the fixed initial amount of acetic acid added to the catalyst. The lower yields of evolved ketonization products from CFe$_3$O$_4$ and CFe$_3$O$_4$-2 h mirrored their weaker acetate band intensities.

3.4.2. Impact of metal impurities

To better understand the role of metal impurities on the performance of reduced FA catalysts, a family of model materials, namely synthetic catalysts in Table S7 were synthesised by doping (and subsequent
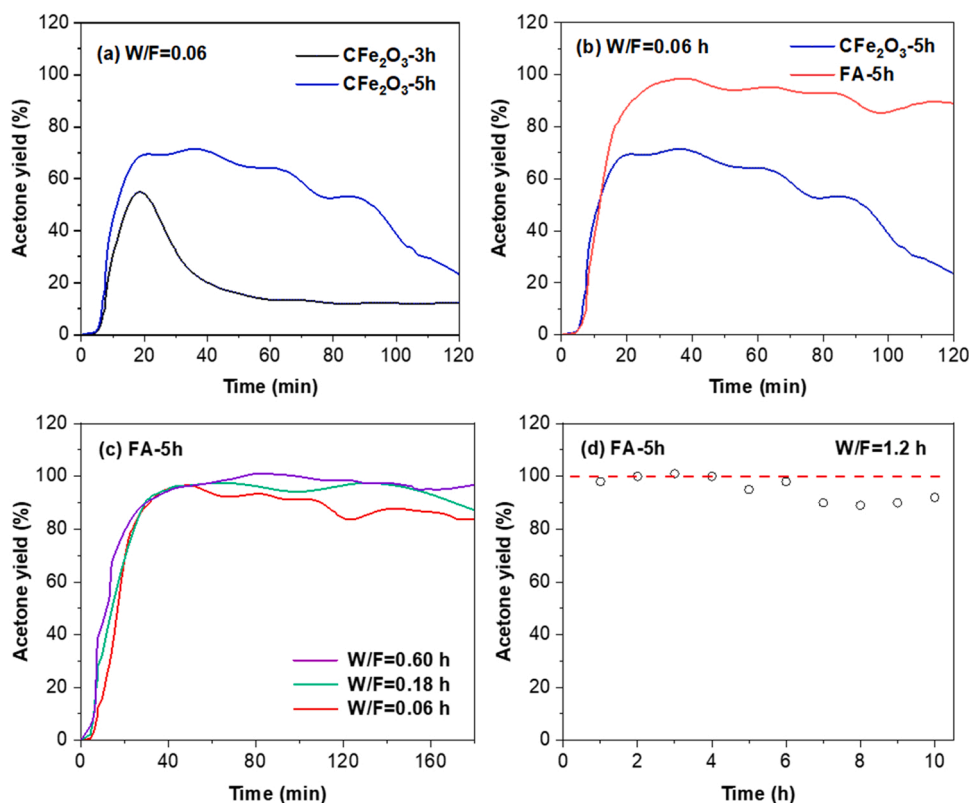
Fig. 7. Acetone yield from acetic acid ketonization as a function of reaction time over reduced commercial Fe_2O_3 and fly ash derived catalysts. Reactions were performed at 400 °C in a plug flow reactor. Acetone yields indirectly determined based on continuously monitored CO_2 yields according to Eq. 1.

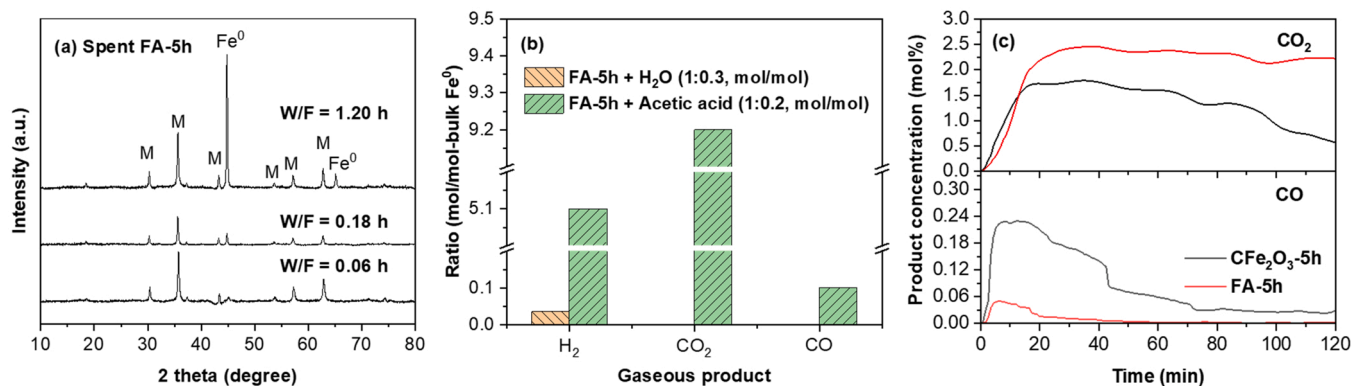**Fig. 8.** (a) XRD of FA-5 h after 5 h acetic acid ketonization at 400 °C from plug flow reactor; (b) gas products of 1 mg FA-5 h with water or acetic acid by Pyroprobe (yields are cumulative from room temperature to 400 °C); (c) evolved CO_2 and CO by-products of acetic acid ketonization over CFe3O4-5 h and FA-5 h at 400 °C and W/F = 0.06 h in the plug flow reactor.

Table 2
Oxygen surface speciation from XPS.

Sample	%			
	$O_{Lattice}$	$O_{Vacancy}$	OH	H_2O^+
FA[a]	68.1	0.6	24.1	7.2
FA-1 h	40.4	16.2	26.1	17.3
FA-3 h	27.6	32.1	28.2	12.1
FA-5 h	26.9	31.4	29.2	12.5
CFe₂O₃-5 h	72.3	3.5	20.4	3.8

[a] Annealed under N_2 at 400 °C for 30 min

annealing and reduction) of commercial hematite. Bulk impurity concentrations of the resulting reduced, synthetic materials being ~8 wt% Al, ~1.4 wt% Mg, ~0.1 wt% Ca and 0.4 wt% Ti, were similar to those of the annealed FA precipitate (Table S3), as intended. Al doping and subsequent thermal processing significantly increased the surface area of the parent hematite from 1 $m^2 \cdot g^{-1}$–23 $m^2 \cdot g^{-1}$, as previously reported for water-gas shift catalysts [54], whereas the additional dopants only conferred a slightly additional increase in surface area (to 35 $m^2 \cdot g^{-1}$).

Carboxylic acid ketonization is proposed to occur through carboxylate adsorption and subsequent α-hydrogen abstraction by Brønsted basic sites (oxygen anions) or keto/enol tautomerisation to form enolates, with proximate Lewis acid sites activating a second carboxylic acid to drive C–C coupling. The acid-base properties of reduced synthetic (Figs. S14-15) and reduced fly ash (Figs. S16-17) materials were
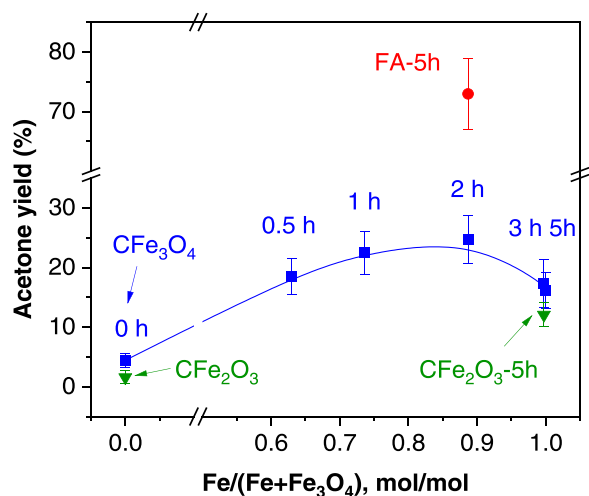
Fig. 9. Acetone yield from acetic acid ketonization versus extent of reduction for commercial magnetite (CFe_3O_4), hematite (CFe_2O_3) and FA-5 h catalysts at 400 °C in a Pyroprobe system; acetone yields are cumulative from room temperature to 400 °C.

therefore characterized by NH_3 and CO_2 TPD. The resulting acid and base site densities are shown in Fig. 11(a-b). Progressive reduction of the annealed FA precipitate from 1 h to 5 h decreased the number of acid sites, but increased the proportion of medium strength acid sites (Table 1). These changes were accompanied by a simultaneous rise in basicity in Fig. 11(a). Reduction of the multi-element fly ash-derived catalysts is complex, since it induces oxygen vacancies in hematite and concomitant formation of Fe^0 species and a magnetite shell (apparent from XPS and XAS), but also promotes surface segregation of more oxophilic metals (e.g. Ca and Mg) to the surface (Fig. 4 and Fig. S7) which are strong bases. It appears that the latter phenomenon more than compensates for oxygen removal which occurs predominantly from iron oxide (magnetite) lattices, resulting in a net increase in surface basicity. A similar phenomenon, oxygen vacancy creation accompanied by increased basicity, is reported for Cu/CeO_2 catalysts for CO_2

hydrogenation to methanol [55]. Ketonization activity (acetone yield) correlates well with the formation of base sites, confirming that Lewis acidity, evidenced by IR of adsorbed pyridine (Fig. S18) alone is insufficient to catalyse the reaction, while FA-5 h offers the optimum balance of Brønsted base and Lewis acid sites. Considering the reduced synthetic materials, the parent hematite (SFe-5 h) possessed very few acid or base sites. Doping hematite with Al (SFeAl-5 h) slightly increased both acidity and basicity (Fig. 11(b), Table S8), while the multiply doped hematite (SFeAlMgCaTi-5 h) material exhibited similar acid/base densities to FA-5 h. The ketonization activity of doped hematites followed their acid-base properties, with the multiply doped SFeAlMgCaTi-5 h catalyst delivering a similar acetone yield to FA-5 h. Clearly, the low concentrations of metal dopants, particularly Ti, can dramatically enhance the reactivity of commercial hematite. In summary, the high activity of FA-5 h appears in large part due to the role of metal dopants in introducing Brønsted basicity into the predominantly Lewis acidic magnetite shell of catalyst nanoparticles.

4. Conclusions

The potential of fly ash waste as a precursor for the synthesis of low cost and sustainable iron catalysts for the upgrading of acidic components of pyrolysis bio-oils was explored. A selective HCl extraction step achieved leaching of ~90 wt% Fe^{3+}, with a subsequent pH switch and annealing resulting in ~1 μm hematite nanoparticles interspersed with ~7 wt% Al and < 1 wt% Mg, Ti and Ca impurities. X-ray spectroscopies evidenced a rapid disproportionation of hematite to magnetite and iron metal on thermal reduction at 400 °C, accompanied by an increase in BET surface area and a significant decrease in particle size. Bulk and surface elemental analysis, and TEM and EDX mapping, are consistent with the formation of ~200 nm Fe metal nanoparticles decorated with large (~80 nm) Fe_3O_4 nanoparticles, in a $Fe@Fe_3O_4$ core-shell structure. XPS indicates the formation of significant surface oxygen vacancies following extended (>1 h) reduction. Reduction-induced restructuring significant enhances both surface acid and base properties, as quantified by NH_3 and CO_2 TPD, with extended (5 h) reduction favouring medium strength Lewis acid sites. The physicochemical changes effected by reduction are mirrored by acetic acid ketonization, with the 5 h reduced
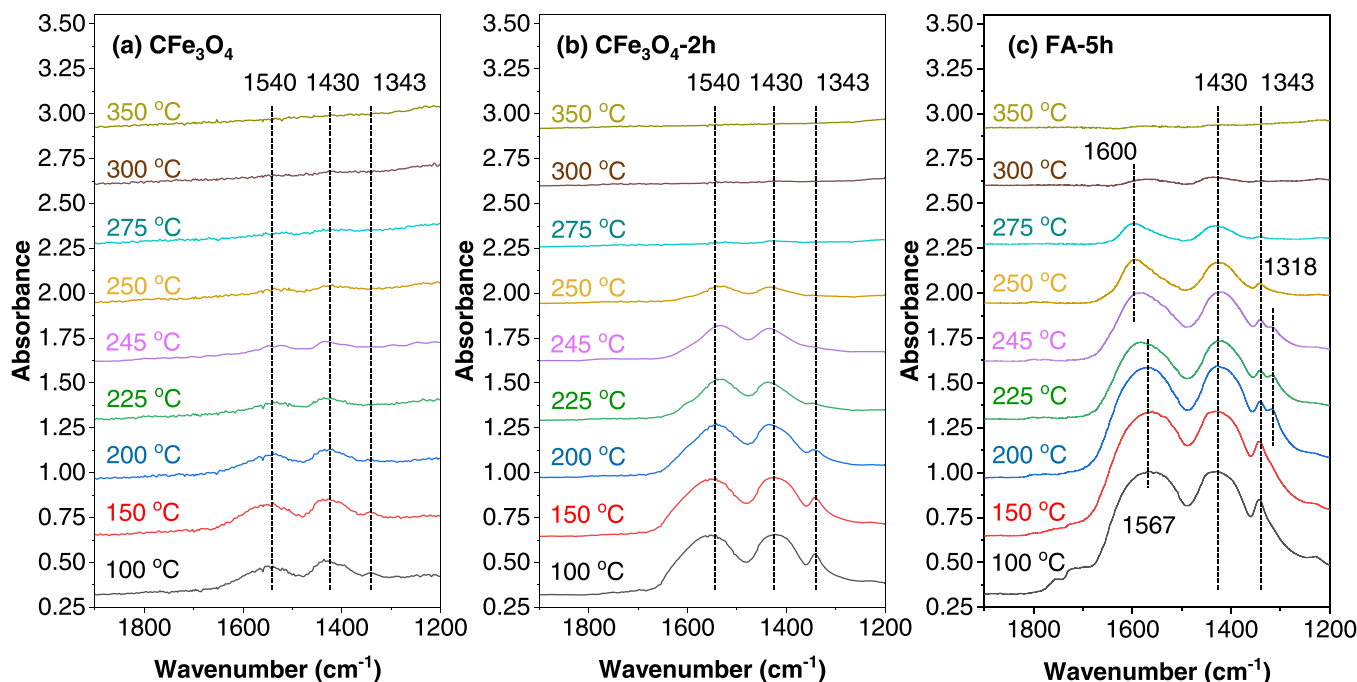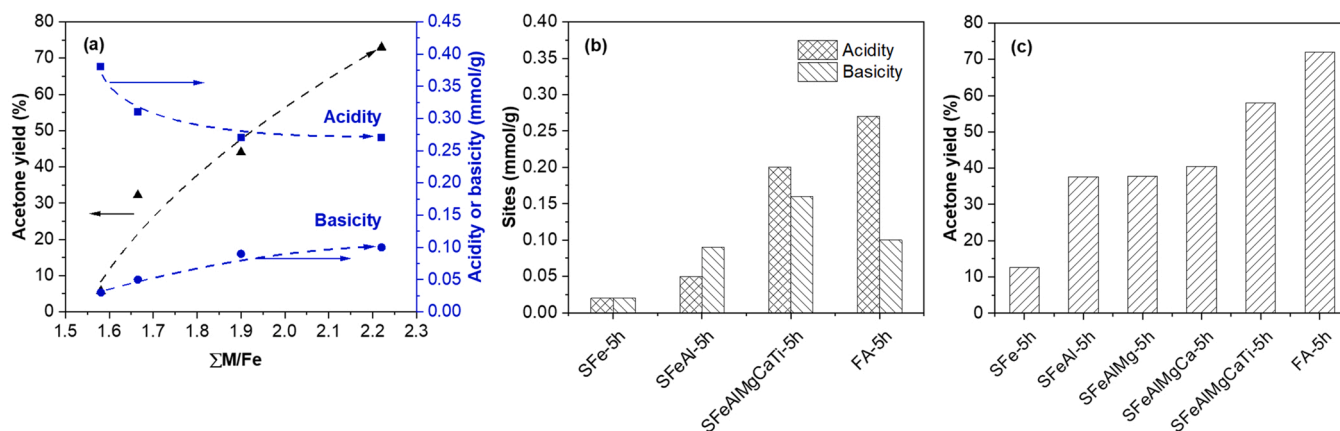

Fig. 10. Temperature programmed DRIFT spectra of acetic acid adsorbed on (a) CFe_3O_4, (b) CFe_3O_4-2 h and (c) FA-5 h.

Fig. 11. (a) Acetone yield and acid/base site densities for FA as a function of relative surface impurity (M) concentration (reduction time, 1–5 h); (b) acid and base site densities of reduced synthetic catalysts; (c) acetone yield of ketonization for reduced synthetic catalysts in Pyroprobe (yields are cumulative from room temperature to 400 °C); Note that all the synthetic catalysts were pre-reduced for 5 h under flowing 10% H_2 at 400 °C.

fly ash derived catalyst (FA-5 h) delivering the highest conversion and acetone yield. Our FA-5 h catalyst significantly outperformed reduced commercial hematite and magnetite, although the latter was the more active of the two pure oxides and activated by prolonged reduction. Temperature-programmed in-situ DRIFTS of chemisorbed revealed a similar bridging, bidentate acetate adsorption mode over FA-5 h and reduced magnetite, with acetate stabilised to a higher temperature (~300 °C) over the fly ash catalyst. Model studies of synthetic, doped hematite confirmed the importance of metal impurities (particularly Al and Ti) in introducing acidity and basicity, and hence promoting ketonization activity. The high activity and on-stream stability of FA-5 h for acetic acid ketonization reflects a combination of a relatively high surface area, oxygen vacancies and mixed Lewis acid/Bronsted base character. It is important to recognise that acetic acid is only one undesirable component present in pyrolysis bio-oils [12,56,57], and hence additional studies are necessary to assess the impact of other corrosive or unstable components, such as hydroxyacetaldehyde, furan and levoglucosan on the performance of our fly ash-derived catalysts, and to establish their stability in extended lifetime tests.

CRediT authorship contribution statement

Sasha Yang: Conceptualization, Investigation, Data curation, Formal analysis, Writing – original draft, Validation. **Binbin Qian:** Methodology, Writing – original draft. **Yuan Wang:** Methodology, Writing – review & editing. **Kenji Taira:** Methodology, Writing – review & editing. **Qiaoqiao Zhou:** Methodology, Writing – review & editing. **Karen Wilson:** Supervision, Resources, Methodology, Writing – review & editing. **Adam F. Lee:** Supervision, Resources, Methodology, Writing – review & editing. **Lian Zhang:** Supervision, Resources, Writing – review & editing, Project administration, Funding acquisition.

Declaration of Competing Interest

The authors declare that they have no known competing financial interests or personal relationships that could have appeared to influence the work reported in this paper.

Data Availability

Data will be made available on request.

Acknowledgements

This work was funded by the Australian Research Council

Appendix A. Supporting information

Supplementary data associated with this article can be found in the online version at doi:10.1016/j.apcatb.2022.122106.

References

[1] Y. Huang, B. Li, D. Liu, X. Xie, H. Zhang, H. Sun, X. Hu, S. Zhang, Fundamental advances in biomass autothermal/oxidative pyrolysis: a review, ACS Sustainable Chemistry & Engineering 8 (2020) 11888–11905, https://doi.org/10.1021/acssuschemeng.0c04196.

[2] P.M. Mortensen, J.D. Grunwaldt, P.A. Jensen, K. Knudsen, A.D. Jensen, A review of catalytic upgrading of bio-oil to engine fuels, Applied Catalysis A: General 407 (2011) 1–19, https://doi.org/10.1016/j.apcata.2011.08.046.

[3] J. Horáček, U. Akhmetzyanova, L. Skuhrovcova, Z. Tišler, H. de Paz Carmona, Alumina-supported MoNx, MoCx and MoPx catalysts for the hydrotreatment of rapeseed oil, Applied Catalysis B: Environmental 263 (2020), 118328, https://doi.org/10.1016/j.apcatb.2019.118328.

[4] T.N. Pham, T. Sooknoi, S.P. Crossley, D.E. Resasco, Ketonization of carboxylic acids: mechanisms, catalysts, and implications for biomass conversion, ACS Catalysis 3 (2013) 2456–2473, https://doi.org/10.1021/cs400501h.

[5] R.W. Snell, B.H. Shanks, Insights into the ceria-catalyzed ketonization reaction for biofuels applications, ACS Catalysis 3 (2013) 783–789, https://doi.org/10.1021/cs400003n.

[6] A.V. Ignatchenko, Multiscale approach for the optimization of ketones production from carboxylic acids by the decarboxylative ketonization reaction, Catalysis Today 338 (2019) 3–17, https://doi.org/10.1016/j.cattod.2019.06.080.

[7] B. Boekaerts, B.F. Sels, Catalytic advancements in carboxylic acid ketonization and its perspectives on biomass valorisation, Applied Catalysis B: Environmental 283 (2021), 119607, https://doi.org/10.1016/j.apcatb.2020.119607.

[8] R. Kumar, N. Enjamuri, S. Shah, A.S. Al-Fatesh, J.J. Bravo-Suarez, B. Chowdhury, Ketonization of oxygenated hydrocarbons on metal oxide based catalysts, Catalysis Today 302 (2018) 16–49, https://doi.org/10.1016/j.cattod.2017.09.044.

[9] Q. Yu, Y. Guo, X. Wu, Z. Yang, H. Wang, Q. Ge, X. Zhu, Ketonization of propionic acid on lewis acidic zr-beta zeolite with improved stability and selectivity, ACS Sustainable Chemistry & Engineering 9 (2021) 7982–7992, https://doi.org/10.1021/acssuschemeng.1c02290.

[10] H. Jahangiri, A. Osatiashtiani, M. Ouadi, A. Hornung, A.F. Lee, K. Wilson, Ga/HZSM-5 catalysed acetic acid ketonisation for upgrading of biomass pyrolysis vapours, Catalysts 9 (2019) 841, https://doi.org/10.3390/catal9100841.

[11] H. Jahangiri, A. Osatiashtiani, J.A. Bennett, M.A. Isaacs, S. Gu, A.F. Lee, K. Wilson, Zirconia catalysed acetic acid ketonisation for pre-treatment of biomass fast pyrolysis vapours, Catalysis Science & Technology 8 (2018) 1134–1141, https://doi.org/10.1039/C7CY02541F.

[12] E. Heracleous, D. Gu, F. Schüth, J.A. Bennett, M.A. Isaacs, A.F. Lee, K. Wilson, A.A. Lappas, Bio-oil upgrading via vapor-phase ketonization over nanostructured FeOx and MnOx: catalytic performance and mechanistic insight, Biomass

Conversion and Biorefinery 7 (2017) 319–329, https://doi.org/10.1007/s13399-017-0268-4.

[13] R. Davis, H.P. Schultz, Studies of thermal decarboxylation of iron carboxylates. i. preparation of symmetrical aliphatic ketones1, 2, The Journal of Organic Chemistry 27 (1962) 854–857, https://doi.org/10.1021/jo01050a039.

[14] D.Y. Murzin, A. Bernas, J. Wärnå, J. Myllyoja, T. Salmi, Ketonization kinetics of stearic acid, Reaction Kinetics, Mechanisms and Catalysis 126 (2019) 601–610, https://doi.org/10.1007/s11144-018-1472-3.

[15] J. Kuriacose, S. Jewur, Studies on the surface interaction of acetic acid on iron oxide, Journal of Catalysis 50 (1977) 330–341, https://doi.org/10.1016/0021-9517(77)90042-2.

[16] L.J. Goossen, P. Mamone, C. Oppel, Catalytic decarboxylative cross-ketonisation of aryl-and alkylcarboxylic acids using magnetite nanoparticles, Advanced Synthesis & Catalysis 353 (2011) 57–63, https://doi.org/10.1002/adsc.201000429.

[17] J.A. Bennett, C.M. Parlett, M.A. Isaacs, L.J. Durndell, L. Olivi, A.F. Lee, K. Wilson, Acetic acid ketonization over Fe$_3$O$_4$/SiO$_2$ for pyrolysis bio-oil upgrading, ChemCatChem 9 (2017) 1648, https://doi.org/10.1002/cctc.201601269.

[18] J. Wrzyszcz, H. Grabowska, R. Klimkiewicz, L. Syper, Catalytic reactions of oxidized n-C10 derivatives over an iron oxide, Applied Catalysis A: General 185 (1999) 153–156, https://doi.org/10.1016/S0926-860X(99)00136-2.

[19] J. Weber, A. Thompson, J. Wilmoth, V.S. Batra, N. Janulaitis, J.R. Kastner, Effect of metal oxide redox state in red mud catalysts on ketonization of fast pyrolysis oil derived oxygenates, Applied Catalysis B: Environmental 241 (2019) 430–441, https://doi.org/10.1016/j.apcatb.2018.08.061.

[20] S. Almutairi, E. Kozhevnikova, I. Kozhevnikov, Ketonisation of acetic acid on metal oxides: catalyst activity, stability and mechanistic insights, Applied Catalysis A: General 565 (2018) 135–145, https://doi.org/10.1016/j.apcata.2018.08.008.

[21] E. Karimi, I.F. Teixeira, L.P. Ribeiro, A. Gomez, R.M. Lago, G. Penner, S.W. Kycia, M. Schlaf, Ketonization and deoxygenation of alkanoic acids and conversion of levulinic acid to hydrocarbons using a Red Mud bauxite mining waste as the catalyst, Catalysis Today 190 (2012) 73–88, https://doi.org/10.1016/j.cattod.2011.11.028.

[22] V. Lorenzelli, G. Busca, N. Sheppard, Infrared study of the surface reactivity of hematite, Journal of Catalysis 66 (1980) 28–35, https://doi.org/10.1016/0021-9517(80)90004-4.

[23] B. Qian, T. Hosseini, X. Zhang, Y. Liu, H. Wang, L. Zhang, Coal waste to two-dimensional materials: Fabrication of α-Fe$_2$O$_3$ nanosheets and MgO nanosheets from brown coal fly ash, ACS Sustainable Chemistry & Engineering 6 (2018) 15982–15982, https://doi.org/10.1021/acssuschemeng.8b03952.

[24] A. Mohajerani, S. Lound, G. Liassos, H. Kurmus, A. Ukwatta, M. Nazari, Physical, mechanical and chemical properties of biosolids and raw brown coal fly ash, and their combination for road structural fill applications, Journal of Cleaner Production 166 (2017) 1–11, https://doi.org/10.1016/j.jclepro.2017.07.250.

[25] T.K. Choo, B. Etschmann, C. Selomulya, L. Zhang, Behavior of Fe$^{2+/3+}$ cation and its interference with the precipitation of Mg^{2+} cation upon mineral carbonation of yallourn fly ash leachate under ambient conditions, Energy & Fuels 30 (2016) 3269–3280, https://doi.org/10.1021/acs.energyfuels.5b02867.

[26] G. Mariotto, S. Murphy, N. Berdunov, S. Ceballos, I. Shvets, Influence of Ca and K on the reconstruction of the Fe$_3$O$_4$ (0 0 1) surface, Surface Science 564 (2004) 79–86, https://doi.org/10.1016/j.susc.2004.06.164.

[27] H. Cho, D. Oh, K. Kim, A study on removal characteristics of heavy metals from aqueous solution by fly ash, Journal of Hazardous Materials 127 (2005) 187–195, https://doi.org/10.1016/j.jhazmat.2005.07.019.

[28] D.K. Ojha, D. Viju, R. Vinu, Fast pyrolysis kinetics of alkali lignin: evaluation of apparent rate parameters and product time evolution, Bioresource Technology 241 (2017) 142–151, https://doi.org/10.1016/j.biortech.2017.05.084.

[29] J.J. Krishna, O.P. Korobeinichev, R. Vinu, Isothermal fast pyrolysis kinetics of synthetic polymers using analytical Pyroprobe, Journal of Analytical and Applied Pyrolysis 139 (2019) 48–58, https://doi.org/10.1016/j.jaap.2019.01.008.

[30] S. Yang, L. Shi, Q. Zhou, B. Qian, A. De Girolamo, L. Zhang, Elucidating the synergistic interaction and reaction pathway between the individual lignocellulosic components during flash pyrolysis, Chemical Engineering Journal 432 (2021), 134372, https://doi.org/10.1016/j.cej.2021.134372.

[31] A. Gumidyala, T. Sooknoi, S. Crossley, Selective ketonization of acetic acid over HZSM-5: The importance of acyl species and the influence of water, Journal of Catalysis 340 (2016) 76–84, https://doi.org/10.1016/j.jcat.2016.04.017.

[32] Z. Yang, Q. Yu, Y. Guo, X. Wu, H. Wang, J. Han, Q. Ge, X. Zhu, Effect of postsynthesis preparation methods on catalytic performance of Ti-Beta zeolite in ketonization of propionic acid, Microporous and Mesoporous Materials 330 (2022), 111625, https://doi.org/10.1016/j.micromeso.2021.111625.

[33] K.C. Chukwu, L. Arnadottir, Density functional theory study of decarboxylation and decarbonylation of acetic acid on Pd (111), The Journal of Physical Chemistry C 124 (2020) 13082–13093, https://doi.org/10.1021/acs.jpcc.0c00436.

[34] B. Qian, C. Liu, J. Lu, M. Jian, X. Hu, S. Zhou, T. Hosseini, B. Etschmann, X. Zhang, H. Wang, Synthesis of in-situ Al^{3+}-defected iron oxide nanoflakes from coal ash: a detailed study on the structure, evolution mechanism and application to water remediation, Journal of Hazardous Materials 395 (2020) 122696, https://doi.org/10.1016/j.jhazmat.2020.122696.

[35] P.R. Anderson, M.M. Benjamin, Surface and bulk characteristics of binary oxide suspensions, Environmental Science & Technology 24 (1990) 692–698, https://doi.org/10.1021/es00075a013.

[36] M. Zhu, I.E. Wachs, Iron-based catalysts for the high-temperature water-gas shift (HT-WGS) reaction: a review, ACS Catalysis 6 (2016) 722–732, https://doi.org/10.1021/acscatal.5b02594.

[37] R. Dieckmann, M. Hilton, T. Mason, Defects and cation diffusion in magnetite (VIII): migration enthalpies for iron and impurity cations, Berichte der Bunsengesellschaft für physikalische Chemie 91 (1987) 59–66, https://doi.org/10.1002/bbpc.19870910113.

[38] S. Benny, High temperature water gas shift catalysts: a computer modelling study, UCL (University College London), 2010.

[39] K.P. Kepp, A quantitative scale of oxophilicity and thiophilicity, Inorganic Chemistry 55 (2016) 9461–9470, https://doi.org/10.1021/acs.inorgchem.6b01702.

[40] N. Cabrera, N.F. Mott, Theory of the oxidation of metals, Reports on Progress in Physics 12 (1949) 163–184, https://doi.org/10.1007/978-1-4684-8920-0_3.

[41] V.P. Zhdanov, Kinetic model of oxidation of metal nanoparticles: Cabrera-Mott and Kirkendall effects, Surface Science 684 (2019) 24–27, https://doi.org/10.1016/j.susc.2018.12.006.

[42] H.J. Fan, U. Gösele, M. Zacharias, Formation of nanotubes and hollow nanoparticles based on kirkendall and diffusion processes: a review, Small 3 (2007) 1660–1671, https://doi.org/10.1002/smll.200700382.

[43] E.O. Kirkendall, Diffusion of zinc in alpha brass, Trans. AIME 104 (1942) 147, https://doi.org/10.31274/rtd-180813-14187.

[44] A. Cabot, V.F. Puntes, E. Shevchenko, Y. Yin, L. Balcells, M.A. Marcus, S. M. Hughes, A.P. Alivisatos, Vacancy coalescence during oxidation of iron nanoparticles, Journal of the American Chemical Society 129 (2007) 10358–10360, https://doi.org/10.1021/ja072574a.

[45] X. Lu, Y. Zeng, M. Yu, T. Zhai, C. Liang, S. Xie, M.S. Balogun, Y. Tong, Oxygen-deficient hematite nanorods as high-performance and novel negative electrodes for flexible asymmetric supercapacitors, Advanced Materials 26 (2014) 3148–3155, https://doi.org/10.1002/adma.201305851.

[46] S. Jain, J. Shah, N.S. Negi, C. Sharma, R.K. Kotnala, Significance of interface barrier at electrode of hematite hydroelectric cell for generating ecopower by water splitting, International Journal of Energy Research 43 (2019) 4743–4755, https://doi.org/10.1002/er.4613.

[47] A. Guntida, T. Rattanachartnarong, B. Jongsomjit, T. Sooknoi, P. Weerachawanasak, S. Praserthdam, P. Praserthdam, Determining the role of oxygen vacancies in palmitone selectivity and coke formation over acid metal oxide catalysts for the ketonization of methyl palmitate, Applied Catalysis A: General 628 (2021) 118405, https://doi.org/10.1016/j.apcata.2021.118405.

[48] S. Tosoni, H.-Y.T. Chen, A. Ruiz Puigdollers, G. Pacchioni, TiO$_2$ and ZrO$_2$ in biomass conversion: why catalyst reduction helps, Philos. Trans. R. Soc. A: Math., Phys. Eng. Sci. 376 (2018) 56, https://doi.org/10.1098/rsta.2017.0056.

[49] A.A. Taimoor, A. Favre-Reguillon, L. Vanoye, I. Pitault, Upgrading of biomass transformation residue: influence of gas flow composition on acetic acid ketonic condensation, Catalysis Science & Technology 2 (2012) 359–363, https://doi.org/10.1039/C1CY00346A.

[50] S. Wang, E. Iglesia, Experimental and theoretical assessment of the mechanism and site requirements for ketonization of carboxylic acids on oxides, Journal of Catalysis 345 (2017) 183–206, https://doi.org/10.1016/j.jcat.2016.11.006.

[51] A.Q. Wang, T.D. Golden, Electrodeposition of oriented cerium oxide films, International Journal of Electrochemistry 2013 (2013), https://doi.org/10.1155/2013/482187.

[52] G. Mekhemer, S. Halawy, M. Mohamed, M. Zaki, Ketonization of acetic acid vapour over polycrystalline magnesia: in situ Fourier transform infrared spectroscopy and kinetic studies, Journal of Catalysis 230 (2005) 109–122, https://doi.org/10.1016/j.jcat.2004.09.030.

[53] M. Tang, W.A. Larish, Y. Fang, A. Gankanda, V.H. Grassian, Heterogeneous reactions of acetic acid with oxide surfaces: effects of mineralogy and relative humidity, The Journal of Physical Chemistry A 120 (2016) 5609–5616, https://doi.org/10.1021/acs.jpca.6b05395.

[54] M. Zhu, I.E. Wachs, Iron-based catalysts for the high-temperature water–gas shift (HT-WGS) reaction: A review, ACS Catalysis 6 (2016) 722–732, https://doi.org/10.1021/acscatal.5b02594.

[55] R. Singh, K. Tripathi, K.K. Pant, Investigating the role of oxygen vacancies and basic site density in tuning methanol selectivity over Cu/CeO$_2$ catalyst during CO$_2$ hydrogenation, Fuel 303 (2021) 121289, https://doi.org/10.1016/j.fuel.2021.121289.

[56] J.C. Manayil, A. Osatiashtiani, A. Mendoza, C.M.A. Parlett, M.A. Isaacs, L. J. Durndell, C. Michailof, E. Heracleous, A. Lappas, A.F. Lee, K. Wilson, Impact of macroporosity on catalytic upgrading of fast pyrolysis bio-oil by esterification over silica sulfonic acids, ChemSusChem 10 (2017) 3506–3511, https://doi.org/10.1002/cssc.201700959.

[57] A. Osatiashtiani, B. Puértolas, C.C.S. Oliveira, J.C. Manayil, B. Barbero, M. Isaacs, C. Michailof, E. Heracleous, J. Pérez-Ramírez, A.F. Lee, K. Wilson, On the influence of Si:Al ratio and hierarchical porosity of FAU zeolites in solid acid catalysed esterification pretreatment of bio-oil, Biomass Conversion and Biorefinery 7 (2017) 331–342, https://doi.org/10.1007/s13399-017-0254-x.